IEEE Access
Multidisciplinary | Rapid Review | Open Access Journal

Received May 10, 2019, accepted May 20, 2019, date of publication May 23, 2019, date of current version June 13, 2019.

Digital Object Identifier 10.1109/ACCESS.2019.2918721

Active Disturbance Rejection With Fast Terminal Sliding Mode Control for a Lower Limb Exoskeleton in Swing Phase

CHAO-FENG CHEN[1], ZHI-JIANG DU[1], (Member, IEEE), LONG HE[2], JIA-QI WANG[1], DONG-MEI WU[1], AND WEI DONG[1], (Senior Member, IEEE)

[1]State Key Laboratory of Robotics and System, Harbin Institute of Technology (HIT), Harbin 150001, China
[2]Weapon Equipment Research Institute, China South Industries Group Corporation, Beijing 102202, China

Corresponding author: Wei Dong (dongwei@hit.edu.cn)

ABSTRACT In this paper, a control strategy is proposed to improve the tracking performance of the lower limb exoskeleton (LLE). The proposed active disturbance rejection control (ADRC) with fast terminal sliding mode control (FTSMC) can not only alleviate the disturbance but also converge to a bounded region fast. Based on the robotics analysis, a dynamic model for the LLE was established. To achieve decoupling control for a coupled system, the virtual control input was introduced, where the system uncertainty and external disturbances were regarded as lumped disturbances. To validate the feasibility of the proposed control strategy, the simulations and experiments were both carried out. The numerical simulation results were shown that the proposed control strategy and ADRC can remarkably reduce the chattering phenomena, which is owing to the estimation ability of extended state observer (ESO). Both the simulations and the experiments results were shown that this strategy was better than the conventional proportional–integral–derivative (PID) and ADRC in terms of tracking performance. With the proposed ADRC-FTSMC, the LLE system can achieve higher tracking precision and faster response.

INDEX TERMS Lower limb exoskeleton, active disturbance rejection, fast terminal sliding mode control, human gait tracking, finite-time convergence.

I. INTRODUCTION

Recently wearable exoskeletons have attracted more research interests due to their wide range of applications such as relieving the heavy rehabilitation work, helping paraplegic or quadriplegic people regain locomotion, empowering healthy people to carry heavy loads, and providing additional power for walking [1]. However, a significant challenging is how to effectively control the exoskeletons to bring its performance into full play [2]. In the past decades, there are several representative exoskeletons designed, and various modeling and control approaches are proposed. Berkeley Lower Extremity Exoskeleton, one of the most famous exoskeletons, uses sensitivity amplification control algorithm to provide most of the assistant force, whose defect is too sensitive to the model uncertainties [3], [4]. Hybrid Assistive Limb is a load carrying and auxiliary walking used exoskeleton system [5], where electromyography signal is employed to predict human-exoskeleton interaction. The limitation of this system is the large noise from the electromyography sensors during walking. Other exoskeletons have been further proposed to produce a virtual modification of the mechanical impedance of the human limbs and to improve their acceleration capabilities through compensating perturbations from the environment [6], [7].

Although great progress has been made in the century-long effort to design and implement robotic exoskeletons, there are still many challenges. Many factors still continue to restrain the performance of exoskeletons, where control strategy is one of the most important issues. In order to tackle the exoskeleton control problem, several approaches have been proposed, e.g., sensitivity amplification [8], predefined gait trajectory control [9], [10], model-based control [11], [12], adaptive control [13], fuzzy control [14], [15], and sliding mode control [16]. These control strategies are used for different exoskeletons and each has its own advantages and disadvantages. Particularly, some control strategies require exact model. Nevertheless, obtaining accurate model is difficult in

The associate editor coordinating the review of this manuscript and approving it for publication was Yangmin Li.

practice, since too many kinematics and dynamics variables are required to recognize by utilizing diverse sensors. Furthermore, the control strategy should reduce the influence from external disturbances to ensure the stability of system. Fuzzy logic method based on back-stepping and learning control has been implemented in upper limb exoskeleton [17] and lower limb exoskeleton [18]. Nevertheless, these methods require a training process.

In order to ensure effective control, some control strategy assumes that all components of the state vector can be obtained by measurement. Whereas this is difficult to realize in some cases. Therefore, it is necessary to estimate unmeasurable states for implementation in the control system. To solve the afore-mentioned problem, some solutions have been proposed. One of the solutions is to extend state observers, which is designed to estimate a wide range of disturbances without an accurate model [19]. With this method, the parametric uncertainties and unmodeled dynamics of the control system are considered as an additional state variable, thus the disturbances and unmodeled dynamics can be compensated by feedback linearization, i.e., active disturbance rejection control (ADRC). The ADRC was presented by Han to provide a solution for disturbances eliminating, which was expected to replace PID strategy due to its superior performance and practical value [20].

ADRC has been implemented with several controllers such as classical PID control [21], sliding mode control for providing robustness [22] and fuzzy control for improving rapid tracking [23]. Besides, the ADRC is also used in the SCARA robot to track a predefined trajectory [24]. All of these applications illustrate the advantages of the ADRC in estimating external disturbances. However, to the authors' knowledge, the contributions about the ADRC employing in the lower limb exoskeleton is not frequently reported.

ADRC is able to restrain the influence of the disturbance and system uncertainty, while it does not improve the response of the system [19]. Furthermore, it is not frequently reported in previous literatures that ADRC is emphasized on the fast convergence. To control the system fast and accurate, the fast terminal sliding mode control (FTSMC) is employed to provide fast response and convergence. Meantime, the chattering caused by the FTSMC can be alleviated, since the ADRC estimates the external disturbances. In view of this, a novel hybrid control strategy based on ADRC and FTSMC is proposed in this paper, which features accuracy, robustness and fast convergence.

The main contributions of the paper are listed as follows. First, the ADRC-FTSMC was proposed to improve the performance of the lower limb exoskeleton through the disturbance estimating and finite-time convergence. Second, the stability and the global convergence property of the designed controller have been proved in this paper. Third, the effectiveness of the proposed method is verified by numerical simulations and experiment studies through comparing with the PID and ADRC method. Fourth, the proposed control strategy is used to track the real-time trajectories of different people.

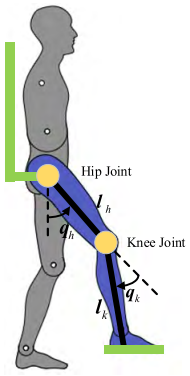

FIGURE 1. The schematic diagram of a wearable exoskeleton for training movement of a subject.

The rest of the paper is organized as follows. In Section 2, the design and mathematical model of the lower limb exoskeleton is presented. A combined active disturbance rejection and fast terminal sliding mode controller is designed in Section 3. Simulation results are shown in Section 4, which illustrates the performance of the proposed control method. Experiments of an LLE prototype using the proposed approach are presented in Section 5. Finally the conclusion and future work is drawn in Section 6.

II. DESIGN AND MODELING OF LOWER LIMB EXOSKELETON

A. DESIGN OF LOWER LIMB EXOSKELETON

In order to achieve comfort walking, the lower limb exoskeleton is designed as a seven degree of freedom (DOF) anthropomorphic device, which has the same DOFs as human lower limb. Specifically, the hip joint consists of an active flexion/extension DOF, a passive internal/external DOF and a passive adduction/abduction DOF. The flexion/extension movement of knee joint is active. The ankle joint has three DOFs, including adduction/abduction DOF, plantar flexion/dorsiflexion DOF and inversion/eversion DOF. All three DOFs of ankle joint are passive. Fig. 2 shows the three main components of the LLE.

1) TRUNK

The trunk of the LLE has two layers: the inner backpack is attached to the human trunk by the shoulder belt and waist belt, while the outer backpack is connected to the LLE waist by the waist adjustment mechanism and gas spring. The inner backpack is connected to the outer backpack by the six-dimensional force sensor (M3715D, SRI, China), which can measure the trunk interaction force between the human and the LLE. The rotation angle of the trunk is measured by the inertial measurement unit (LPMS-CU2, ALUBI, China). Through the adjustment mechanism, the length of the LLE waist can be adjusted from 340mm to 400mm. The stiffness of the gas spring is 10N/mm, which is capable of supporting the mechanism. Besides, thanks to the elasticity, the impact

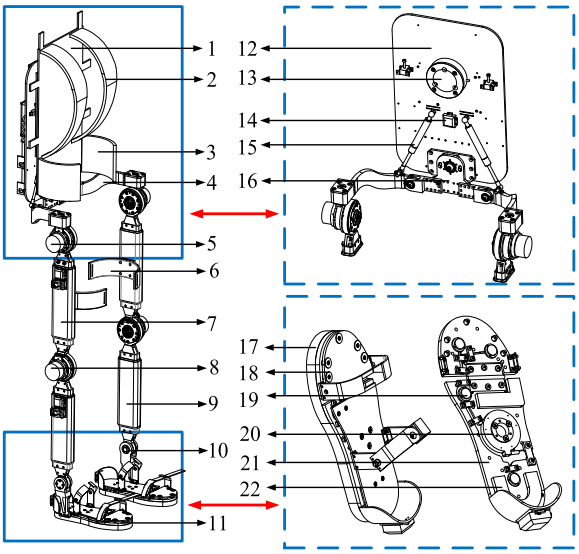

FIGURE 2. Mechanical structure of the exoskeleton. 1: inner backpack, 2: shoulder belt, 3: waist belt, 4: waist connecting part, 5: hip joint, 6: thigh attachment, 7: thigh segment, 8: knee joint, 9: shank segment, 10: ankle joint, 11: wearable shoes, 12: outer backpack, 13: six-dimensional force sensor on backpack, 14: inertial measurement unit, 15: gas spring, 16: waist adjustment part, 17: lower sole of wearable shoes, 18: upper sole of wearable shoes, 19: pressure sensor, 20: six-dimensional force sensor on wearable shoes, 21: middle sole of wearable shoes, 22: rubber insert.

is relieved. The back of the outer backpack is equipped with the control enclosure, the power unit, and other equipment.

2) LEG SEGMENT

The leg segment consists of a thigh, a shank, and three joints. Hip and knee flexion joints are actuated by a harmonic drive (LHD, LEADERDRIVE, China) equipped with electrical brushless motors (EC60, MAXON, Switzerland), which can produce extension/flexion motions in sagittal plane. The peak and average torques provided by the actuated joints are 54Nm and 24Nm respectively at the speed higher than 46rpm. The passive ankle joint connects the shank segment to the wearable shoes by a curved ball bearing. Both the thigh and the shank is made of carbon fiber and the weight of one leg is 6.5 kg. The thigh attachment, which is attached to the human leg, is fixed to thigh segment. The adjustment mechanism, which connects the joint to the thigh and the shank, is designed to fit the users whose height range is from 168 cm to 188 cm. The length of the thigh segment can be adjusted from 360 mm to 400 mm while the shank segment can be adjusted from 340 mm to 380 mm.

3) WEARABLE SHOES

The wearable shoes has three layers, i.e., the upper sole, the middle sole and the lower sole. The upper sole that is made of aluminum alloy contacts with subject's shoes. The middle sole, which is used to measure the foot interaction force between the subject's shoes and the wearable shoes of LLE, consists of four pressure sensors (AT8106, AUTODA, China) and a six-dimensional force sensor (M3554E, SRI, China). The lower sole made of rubber is to relieve impact and to enhance the flexibility. The middle sole is connected with the upper sole through the six-dimensional force sensor. Besides, some rubber materials are inserted into the middle sole to protect the sensors. The middle sole is fixed on the lower sole through the bolts. To make the wearable shoes comfortable, the upper and the middle sole are divided into two revolved connected parts.

TABLE 1. Nomenclature.

Notation	Description
$\boldsymbol{M}_h(\boldsymbol{q})$, $\boldsymbol{M}_k(\boldsymbol{q})$	The inertia matrices of the thigh segment and the shank segment respectively
$\boldsymbol{C}_h(\boldsymbol{q})$, $\boldsymbol{C}_k(\boldsymbol{q})$	The Coriolis and centrifugal force matrices of the thigh segment and the shank segment respectively
$\boldsymbol{G}_h(\boldsymbol{q})$, $\boldsymbol{G}_k(\boldsymbol{q})$	The gravitational items of the thigh segment and the shank segment respectively
$\boldsymbol{D}_1$, $\boldsymbol{D}_2$	The external disturbances and un-modeled dynamics
m_h, m_k	Masses of the thigh segment and the shank segment respectively
l_h, l_k	Lengths of the thigh and the shank respectively
q_h, q_k	Defined joint angles of hip and knee respectively
g	The gravity constant
$\boldsymbol{T}_h$, $\boldsymbol{T}_k$	Torques generated by hip and knee of the exoskeleton respectively

B. MODELING OF LOWER LIMB EXOSKELETON

Due to the periodicity of human lower limb motion in daily life, the paper mainly focuses on the exoskeleton gait during swing phase to assist the human lower limb movement.

According to the biomechanics and dynamics of human gait [25], the normal gait can be generally divided into several distinct phases. Concerning single leg, the basic divisions of the gait cycle can be divided into a stance phase for load transfer and a swing phase for unloaded movement. Fig. 1 presented the schematic diagram of a wearable exoskeleton system, where a human leg attached with a wearable exoskeleton in a swing movement is depicted. The wearable exoskeleton is powered by two actuators which exports and transfers torque to the knee joint and hip joint respectively. The belt in the exoskeleton binds the human leg to guarantee the stability of the human-machine system. The physical parameters of each segment are listed in Table 1.

The human lower limb has three joints, i.e., hip joint, knee joint, and ankle joint. In order to analyze the gait characteristics of the lower limb exoskeleton, we simplify the model and make the following assumptions. First, the lower limb exoskeleton moves on the sagittal plane, based on which, the hip and knee joints can be considered as the rotation joints that move around a fixed axis. Second, giving that the travelling range of the ankle joint is small in sagittal plane, the ankle joint is regarded as a fixed joint in the model. Third, because of symmetry, only one leg is considered in the

mathematical model. Fourth, since we mainly study the swinging legs, the trunk can be regarded as a fixed position. Finally, we consider the mass and length of exoskeleton is constant, since it is more close to realistic physical configurations. According to the Euler-Lagrange equations [26], the dynamic model of the whole system can be described as below,

$$\boldsymbol{M}(\boldsymbol{q})\ddot{\boldsymbol{q}} + \boldsymbol{C}(\boldsymbol{q}, \dot{\boldsymbol{q}})\dot{\boldsymbol{q}} + \boldsymbol{G}(\boldsymbol{q}) + \boldsymbol{D} = \boldsymbol{T} \tag{1}$$

where $\boldsymbol{q} = \left[q_h, q_k\right]^T$, $\dot{\boldsymbol{q}} = \left[\dot{q}_h, \dot{q}_k\right]^T$, $\ddot{\boldsymbol{q}} = \left[\ddot{q}_h, \ddot{q}_k\right]^T$ are the angle, velocity and acceleration of the hip and knee joints respectively; $\boldsymbol{M}(\boldsymbol{q}) \in \boldsymbol{R}^{2\times2}$ is the symmetric definite inertial matrix, which is function of $\boldsymbol{q}$; $\boldsymbol{C}(\boldsymbol{q}, \dot{\boldsymbol{q}}) \in \boldsymbol{R}^{2\times2}$ is the Coriolis and centrifugal force matrix, which is function of $\boldsymbol{q}$ and $\dot{\boldsymbol{q}}$; $\boldsymbol{G}(\boldsymbol{q}) \in \boldsymbol{R}^{2\times1}$ is the gravitational force matrix, which is function of $\boldsymbol{q}$; $\boldsymbol{D} \in \boldsymbol{R}^{2\times1}$ denotes un-modeled dynamics and external disturbances; $\boldsymbol{T} = [\boldsymbol{T}_h, \boldsymbol{T}_k]^T$ denotes the output torques of the exoskeleton at the knee and hip joints (the ankle joint of the exoskeleton is passive).

For Eq. (1), three properties are presented as the following [27].

1. Matrix $\boldsymbol{M}(\boldsymbol{q})$ is symmetric and positive definite.

2. Matrix $\boldsymbol{M}(\boldsymbol{q}) - 2\boldsymbol{C}(\boldsymbol{q}, \dot{\boldsymbol{q}})$ is a skew-symmetric matrix if $\forall \boldsymbol{\varepsilon} \in \boldsymbol{R}^2$, $\boldsymbol{\varepsilon}^T(\boldsymbol{M}(\boldsymbol{q}) - 2\boldsymbol{C}(\boldsymbol{q}, \dot{\boldsymbol{q}}))\boldsymbol{\varepsilon} = 0$.

3. There exist finite scalars $\delta_i > 0$, $i = 1, \ldots, 4$ such that $\|\boldsymbol{M}(\boldsymbol{q})\| \le \delta_1$, $\|\boldsymbol{C}(\boldsymbol{q}, \dot{\boldsymbol{q}})\| \le \delta_2$, $\|\boldsymbol{G}(\boldsymbol{q})\| \le \delta_3$, and $\|\boldsymbol{D}\| \le \delta_4$, which means all items in dynamic model are bounded.

The specific expression of matrices $\boldsymbol{M}(\boldsymbol{q})$, $\boldsymbol{C}(\boldsymbol{q}, \dot{\boldsymbol{q}})$ and $\boldsymbol{G}(\boldsymbol{q})$ can be shown as follows.

$$\begin{cases} \boldsymbol{M}(\boldsymbol{q}) = \begin{bmatrix} \boldsymbol{M}_h(\boldsymbol{q}) \\ \boldsymbol{M}_k(\boldsymbol{q}) \end{bmatrix} = \begin{bmatrix} M_{11} & (q)\, M_{12}\,(q) \\ M_{21} & (q)\, M_{22}\,(q) \end{bmatrix} \\ \boldsymbol{C}(\boldsymbol{q}, \dot{\boldsymbol{q}}) = \begin{bmatrix} \boldsymbol{C}_h(\boldsymbol{q}, \dot{\boldsymbol{q}}) \\ \boldsymbol{C}_k(\boldsymbol{q}, \dot{\boldsymbol{q}}) \end{bmatrix} = \begin{bmatrix} C_{11}\,(q, \dot{q}) & C_{12}\,(q, \dot{q}) \\ C_{21}\,(q, \dot{q}) & C_{22}\,(q, \dot{q}) \end{bmatrix} \\ \boldsymbol{G}(\boldsymbol{q}) = \begin{bmatrix} \boldsymbol{G}_h(\boldsymbol{q}) \\ \boldsymbol{G}_k(\boldsymbol{q}) \end{bmatrix} = \begin{bmatrix} G_1\,(q) \\ G_2\,(q) \end{bmatrix} \end{cases} \tag{2}$$

The inertial matrix $\boldsymbol{M}(\boldsymbol{q})$ can be represented as below.

$$\begin{aligned} M_{11}\,(q) &= \frac{1}{3}m_h l_h^2 + m_k l_h^2 + \frac{1}{3}m_k l_k^2 + m_k l_h l_k \cos q_k \\ M_{12}\,(q) &= -\frac{1}{3}m_k l_k^2 - \frac{1}{2}m_k l_h l_k \cos q_k \\ M_{21}\,(q) &= -\frac{1}{3}m_k l_k^2 - \frac{1}{2}m_k l_h l_k \cos q_k \\ M_{22}\,(q) &= \frac{1}{3}m_k l_k^2 \end{aligned} \tag{3}$$

The Coriolis and centrifugal force matrix $\boldsymbol{C}(\boldsymbol{q})$ can be represented as followings.

$$\begin{aligned} C_{11}\,(q) &= -m_k l_h l_k \dot{q}_k \sin q_k \\ C_{12}\,(q) &= \frac{1}{2}m_k l_h l_k \dot{q}_k \sin q_k \\ C_{21}\,(q) &= \frac{1}{2}m_k l_h l_k \dot{q}_h \sin q_k \\ C_{22}\,(q) &= 0 \end{aligned} \tag{4}$$

The gravitational item $\boldsymbol{G}(\boldsymbol{q})$ can be represented as below.

$$\begin{aligned} G_1\,(q) &= \frac{1}{2}m_h g l_h \sin q_h + m_k g l_h \sin q_h + \frac{1}{2}m_k g l_k \sin(q_h - q_k) \\ G_2\,(q) &= -\frac{1}{2}m_k g l_k \sin(q_h - q_k) \end{aligned} \tag{5}$$

Note that these equations apply to the case where the torso is stationary. The experiments studies in this paper are all performed under this case.

Meanwhile, $\boldsymbol{q}_h^d$ denotes the expected input angles of the thigh with respect to the torso, and $\boldsymbol{q}_k^d$ is the one of the shank with respect to the thigh.

The aim of designing an effective controller is to ensure that the state variables $\boldsymbol{q}_h$ and $\boldsymbol{q}_k$ can track $\boldsymbol{q}_h^d$ and $\boldsymbol{q}_k^d$ precisely and quickly.

III. DESIGN OF GUIDANCE LAWS

A. DECOUPLING BETWEEN THE HIP JOINT AND THE KNEE JOINT

In this paper, the dynamic model of the exoskeleton leg is a multi-input and multi-output (MIMO) system. Eq. (1) can be expressed in the following form.

$$\begin{cases} M_{11}\ddot{q}_h + M_{12}\ddot{q}_k + C_{11}\dot{q}_h + C_{12}\dot{q}_k + G_1 + D_1 = T_h \\ M_{21}\ddot{q}_h + M_{22}\ddot{q}_k + C_{21}\dot{q}_h + C_{22}\dot{q}_k + G_2 + D_2 = T_k \end{cases} \tag{6}$$

Eq. (6) can be further formulated as below,

$$\begin{bmatrix} \ddot{q}_h \\ \ddot{q}_k \end{bmatrix} = \begin{bmatrix} f_1 \\ f_2 \end{bmatrix} + \begin{bmatrix} b_{11} & b_{12} \\ b_{21} & b_{22} \end{bmatrix} \begin{bmatrix} T_h \\ T_k \end{bmatrix} \tag{7}$$

with

$$\boldsymbol{B} = \begin{bmatrix} b_{11} & b_{12} \\ b_{21} & b_{22} \end{bmatrix} = \begin{bmatrix} \dfrac{M_{22}}{W} & -\dfrac{M_{12}}{W} \\ -\dfrac{M_{21}}{W} & \dfrac{M_{11}}{W} \end{bmatrix}.$$

W is derived as,

$$W = M_{11}M_{22} - M_{12}M_{21} \tag{8}$$

In Eq. (7), $\boldsymbol{f} = \begin{bmatrix} f_1 & f_2 \end{bmatrix}^T$ is the coupled term which can be expressed as Eq. (9)

$$\begin{aligned} f_1 &= \frac{1}{W}\left[(M_{12}C_{21} - M_{22}C_{11})\,\dot{q}_h + (M_{12}C_{22} - M_{22}C_{12})\,\dot{q}_k \right. \\ &\quad \left. + (M_{12}G_2 - M_{22}G_1)\right] + \frac{1}{W}(M_{12}D_2 - M_{22}D_1) \\ &= f_{10} + f_{1d} \\ f_2 &= -\frac{1}{W}\left[(M_{21}C_{11} - M_{11}C_{21})\,\dot{q}_h + (M_{11}C_{22} - M_{21}C_{12})\,\dot{q}_k \right. \\ &\quad \left. + (M_{11}G_2 - M_{21}G_1)\right] - \frac{1}{W}(M_{11}D_2 - M_{21}D_1) \\ &= f_{20} + f_{2d} \end{aligned} \tag{9}$$

Note that, $\boldsymbol{f}_0 = [f_{10}\, f_{20}]^T$ is a given vector that is caused by inertia and gravity; $\boldsymbol{f}_d = \begin{bmatrix} f_{1d} & f_{2d} \end{bmatrix}^T$ represents system uncertainties and external disturbances that are hard to be determined directly.

By introducing virtual control variable $\boldsymbol{U} = \begin{bmatrix} u_1 & u_2 \end{bmatrix}^T$, where $u_1 = b_{11}T_h + b_{12}T_k$, $u_2 = b_{21}T_h + b_{22}T_k$, Eq. (7) can be rewritten as below,

$$\begin{cases} \ddot{q}_h = f_{10} + f_{1d} + u_1 \\ \ddot{q}_k = f_{20} + f_{2d} + u_2 \\ y_1 = q_h \\ y_2 = q_k \end{cases} \tag{10}$$

where u_i is the i^{th} ($i = 1, 2$) input channel and $[y_1\ y_2]^T = [q_h\ q_k]^T$ is the corresponding output. In this way, the system is decoupled where two independent SISO systems are obtained.

The actual control torque can be expressed as below.

$$\begin{bmatrix} T_h \\ T_k \end{bmatrix} = \begin{bmatrix} b_{11} & b_{12} \\ b_{21} & b_{22} \end{bmatrix}^{-1} \begin{bmatrix} u_1 \\ u_2 \end{bmatrix} = \boldsymbol{B}^{-1}\boldsymbol{U} \tag{11}$$

After decoupling the system, ADRC can be designed for each channel individually.

B. ADRC FOR THE LOWER LIMB EXOSKELETON

The ADRC treats the system model uncertainties and external disturbances as an extended state, which can be equally compensated in the controller to realize the dynamics compensation.

To improve the noise resistance and robustness of the system in some special situations [32], the Tracking Differentiator (TD) was used to resolve the problem of differential signal extraction via integration. Besides, TD has the ability to track input reference signal with quick response and without overshooting. A feasible second-order TD can be design as below,

$$\begin{aligned} \dot{v}_1 &= v_2 \\ \dot{v}_2 &= fhan\left(v_1 - v\left(t\right), v_2, r, h_0\right) \end{aligned} \tag{12}$$

where $v\left(t\right)$ denotes the control objective; r is the control parameter which determines the tracking speed, and h_0 is the control parameter which impacts the filtering performance. The function $fhan\left(v_1 - v\left(t\right), v_2, r, h_0\right)$ is defined as follows,

$$fhan = -r\left(\frac{a}{d} - sgna\right)s_a - r\text{sgn}a \tag{13}$$

where a, d, s_a can be represented by r and h_0, which described in [20].

Based on Eq. (10), the decoupled system can be expressed as follows,

$$\ddot{\boldsymbol{q}}(t) = \boldsymbol{f}_0\left(\dot{q}_h(t), \dot{q}_k(t), q_h(t), q_k(t)\right) + \boldsymbol{f}_d(w(t)) + \boldsymbol{u}(t) \tag{14}$$

where $\boldsymbol{u}(t)$ and $\ddot{\boldsymbol{q}}(t)$ are the input and output of the system, respectively; $w(t)$ is the external disturbance. Assuming $\boldsymbol{f}_d(w(t))$ is differentiable, which represents the nonlinear time-varying dynamics of the lower limb exoskeleton, the system can be rewritten as the following expression,

$$\begin{cases} \dot{x}_1 = x_2 \\ \dot{x}_2 = f_{10}(x) + f_{1d}(w) + u_1 \\ \dot{x}_3 = d_1(x, w, iv) \\ y_1 = x_1 \end{cases}$$
$$\begin{cases} \dot{x}_4 = x_5 \\ \dot{x}_5 = f_{20}(x) + f_{2d}(w) + u_2 \\ \dot{x}_6 = d_2(x, w, w) \\ y_2 = x_4 \end{cases} \tag{15}$$

where $\boldsymbol{x} = [x_1, x_2, x_3, x_4, x_5, x_6]^T$, $\boldsymbol{u} = [u_1, u_2]$ and $\boldsymbol{y} = [y_1, y_2]$ are respectively the state, input and output of the system and $\boldsymbol{d}(x, w, \dot{w}) = \dot{\boldsymbol{f}}_d$. Then, a third-order ESO can be designed as Eq. (16),

$$\begin{cases} e_1 = \hat{x}_1 - x_1 \\ \dot{\hat{x}}_1 = \hat{x}_2 - \gamma_1 e_1 \\ \dot{\hat{x}}_2 = u_1 + f_{10}(x) + \hat{x}_3 - \gamma_2 e_1 \\ \dot{\hat{x}}_3 = -\gamma_3 e_1 \end{cases}$$
$$\begin{cases} e_2 = \hat{x}_4 - x_4 \\ \dot{\hat{x}}_4 = \hat{x}_5 - \gamma_4 e_2 \\ \dot{\hat{x}}_5 = u_2 + f_{20}(x) + \hat{x}_6 - \gamma_5 e_2 \\ \dot{\hat{x}}_6 = -\gamma_6 e_2 \end{cases} \tag{16}$$

where $\hat{x}_1$, $\hat{x}_2$, $\hat{x}_4$, $\hat{x}_5$ are the estimation of x_1, x_2, x_4, x_5 and $\hat{x}_3$, $\hat{x}_6$ are used to estimate $d_1(t)$ and $d_2(t)$. $L_1 = \begin{bmatrix} \gamma_1 & \gamma_2 & \gamma_3 \end{bmatrix}^T$ and $L_2 = \begin{bmatrix} \gamma_4 & \gamma_5 & \gamma_6 \end{bmatrix}^T$ are the observer gain parameters. The observer gains are chosen such that the characteristic polynominal $s^3 + \gamma_1 s^2 + \gamma_2 s + \gamma_3$ and $s^3 + \gamma_4 s^2 + \gamma_5 s + \gamma_6$ are Hurwitz-type. The bandwidth of all the observers is defined as the same value of $-\omega_0$ for tuning simplicity. It results in that Eq. (16) can be formulated as the characteristic polynominal form,

$$\begin{aligned} s^3 + \gamma_1 s^2 + \gamma_2 s + \gamma_3 &= (s + \omega_0)^3 \\ s^3 + \gamma_4 s^2 + \gamma_5 s + \gamma_6 &= (s + \omega_0)^3 \end{aligned} \tag{17}$$

where the observer bandwidtch ω_0 is the single tuning parameter. If the observer gain vectors $L_1 = \begin{bmatrix} 3\omega_0 & 3\omega_0^2 & \omega_0^3 \end{bmatrix}^T$ and $L_2 = \begin{bmatrix} 3\omega_0 & 3\omega_0^2 & \omega_0^3 \end{bmatrix}^T$ are properly selected, an excellent tracking performance can be guaranteed.

$$\begin{aligned} \hat{x}_1 &\to q_h, \hat{x}_2 \to \dot{q}_h, \hat{x}_3 \to f_{1d}(x, w) \\ \hat{x}_4 &\to q_k, \hat{x}_5 \to \dot{q}_k, \hat{x}_6 \to f_{2d}(x, w) \end{aligned} \tag{18}$$

Generally, within the appropriate range, lager observer bandwidth ω_0 means the more accurate estimation of the control system. However, on the other hand, larger observer bandwidth also leads the system to noise sensitivity. Hence, a tradeoff should be made to seek a balance between tracking performance and the capability of noise tolerance [28].

Once the observer bandwidth is well adjusted, the output of the system will track x_1, x_2, x_3, x_4, x_5 and x_6. Besides,

the ADRC actively compensates for $f_{1d}(x, w)$ and $f_{2d}(x, w)$ in real time. The ADRC control strategy is given by

$$\boldsymbol{T}_{ADRC} = [T_1 T_2]^T = \boldsymbol{B}^{-1} \cdot \left(\boldsymbol{K}_p \boldsymbol{e} + \boldsymbol{K}_d \dot{\boldsymbol{e}}\right) - \boldsymbol{f}_d \quad (19)$$

where $\boldsymbol{e}$ and $\dot{\boldsymbol{e}}$ are the state estimation error of position and velocity respectively.

C. ADRC-FTSMC DESIGNED FOR THE LOWER LIMB EXOSKELETON

The method of determining $\boldsymbol{K}_p$ and $\boldsymbol{K}_d$ was proposed in [28], where the bandwidth thought is used, but its physical meaning is not clear. Furthermore, the tracking is hard to achieve perfect performance in the finite time. Therefore, the fast terminal sliding mode control method is used to the design of error feedback control law in this section.

Assuming the desired reference value is $\boldsymbol{q}^d = \left[\boldsymbol{q}_h^d, \boldsymbol{q}_k^d\right]^T$, the tracking error can be formulated as below:

$$\boldsymbol{e} = \begin{bmatrix} \boldsymbol{e}_1 \\ \boldsymbol{e}_2 \end{bmatrix} = \begin{bmatrix} \boldsymbol{q}_h - \boldsymbol{q}_h^d \\ \boldsymbol{q}_k - \boldsymbol{q}_k^d \end{bmatrix} \quad (20)$$

The FTSMC proposed in [29] is adopted as follows,

$$S = \dot{e} + \alpha e + \beta e^{\frac{q}{p}} \quad (21)$$

where $S = [S_1, S_2]^T$, α and β are positive integers, p and q are positive odd numbers. By properly choosing p and q, given an initial state $e(0) \neq 0$, Eq. (21) will reach $e = 0$ in finite time. The convergence time along the sliding mode surface t_f can be obtained as follows [30],

$$t_f = \frac{1}{\alpha(1 - q/p)} \ln \frac{\alpha(e(0))^{1-q/p} + \beta}{\beta} \quad (22)$$

where $e(0) = q(0) - q_d(0)$.

Based on the sliding mode structure theory, the time derivative of S along with the trajectories of the system Eq. (10) leads to

$$\dot{S} = \ddot{e} + \alpha \dot{e} + \beta \frac{q}{p} e^{q/p} \dot{e} \quad (23)$$

Replacing $\ddot{e}$ by its expression in Eq. (20), it yields to

$$\dot{S} = \ddot{q} - \ddot{q}_d + \alpha \dot{e} + \beta \frac{q}{p} e^{q/p} \dot{e} \quad (24)$$

with $\ddot{q} = f_0 + f_d + u$.

The exponent reaching law is given as follows [31].

$$\dot{S} = -\varepsilon \operatorname{sgn} S - kS \quad (25)$$

The function sgn S is given by $\operatorname{sgn} S = S/(|S| + \xi)$ which is used to guarantee the sliding motion will be close to sliding surface (S = 0). Combine Eq. (24) and Eq. (25).

$$(f_0 + f_d + u - \ddot{q}_d) + \alpha \dot{e} + \beta \frac{q}{p} e^{q/p} \dot{e} = -\varepsilon \operatorname{sgn} S - kS \quad (26)$$

Design the total control u as follows.

$$u = -\varepsilon \operatorname{sgn} S - kS - \alpha \dot{e} - \beta \frac{q}{p} e^{q/p} \dot{e} - f_0 - f_d + \ddot{q}_d \quad (27)$$

With the system uncertainty and external disturbance f_d estimated by the ESO in Eq. (16), the compound control law is modified as follows,

$$u = -\varepsilon \operatorname{sgn} S - kS - \alpha \dot{e} - \beta \frac{q}{p} e^{q/p} \dot{e} - f_0 - x_d + \ddot{q}_d \quad (28)$$

where $x_d = \begin{bmatrix} x_3 & x_6 \end{bmatrix}^T$.

Consider the Lyapunov function as following.

$$V = \frac{1}{2} S^2 \quad (29)$$

Its time derivative is formulated as below,

$$\begin{aligned} \dot{V} &= S\dot{S} = S\left(\ddot{q} - \ddot{q}_d + \alpha \dot{e} + \beta \frac{q}{p} e^{q/p} \dot{e}\right) \\ &= S\left(f_0 + f_d + u - \ddot{q}_d + \alpha \dot{e} + \beta \frac{q}{p} e^{q/p} \dot{e}\right) \\ &= S\left(-\varepsilon \operatorname{sgn} S - kS + f_d - x_d\right) \\ &\leq -kS^2 - (\varepsilon - (f_d - x_d))\,|S| \end{aligned} \quad (30)$$

where $f_d - x_d$ is the residual error from ESO. The fundamental selection of the parameters can be chosen as $k > 0$, and $\varepsilon > f_d - x_d$. The estimation errors will be smaller via tuning the parameters of ESO. It is obvious that $\dot{V}$ is negative. According to Lyapunov stability theory, the system is stable. Fig. 3 shown the structure of ADRC-FTSMC control. In this study, we combined the two parts in LLE to provide fast and accurate response, and significantly reduce the chattering.

Remark 1: Since the disturbance has been precisely estimated by the ADRC, the magnitude of the estimation error will converge to finite range. This will alleviate the chattering phenomenon.

Remark 2: The sliding mode surface can make the system trajectory converge quickly. According to Eq. (22), the proposed control strategy shows finite-time convergence.

IV. SIMULATIONS

In this section, simulation studies are presented to evaluate the effectiveness of the proposed control strategy, where the PID control and active disturbance rejection control (ADRC) are utilized in comparison group. The simulations are implemented applying MATLAB/SIMULINK. The desired trajectories of the hip joint and knee joint come from the clinical gait analysis (CGA). Based on this, the following fitting functions can be obtained.

$$\begin{cases} q_h(t) = 3.85\cos(0.330t + 2.14) \\ \qquad\quad +71.6\cos(3.49t - 1.88) \\ \qquad\quad +41.0\cos(4.68t - 0.3) \\ q_k(t) = 40.9\cos(1.04t - 0.208) \\ \qquad\quad +157\cos(5.82 - 0.047) \\ \qquad\quad +82.3\cos(7.49t - 4.13) \end{cases} \quad (31)$$

The applied torque is calculated by three control methods, respectively. The external disturbance is generated in a random way (between −1 and 1). The sampling time is 0.001s. The physical parameters used in the exoskeleton are given

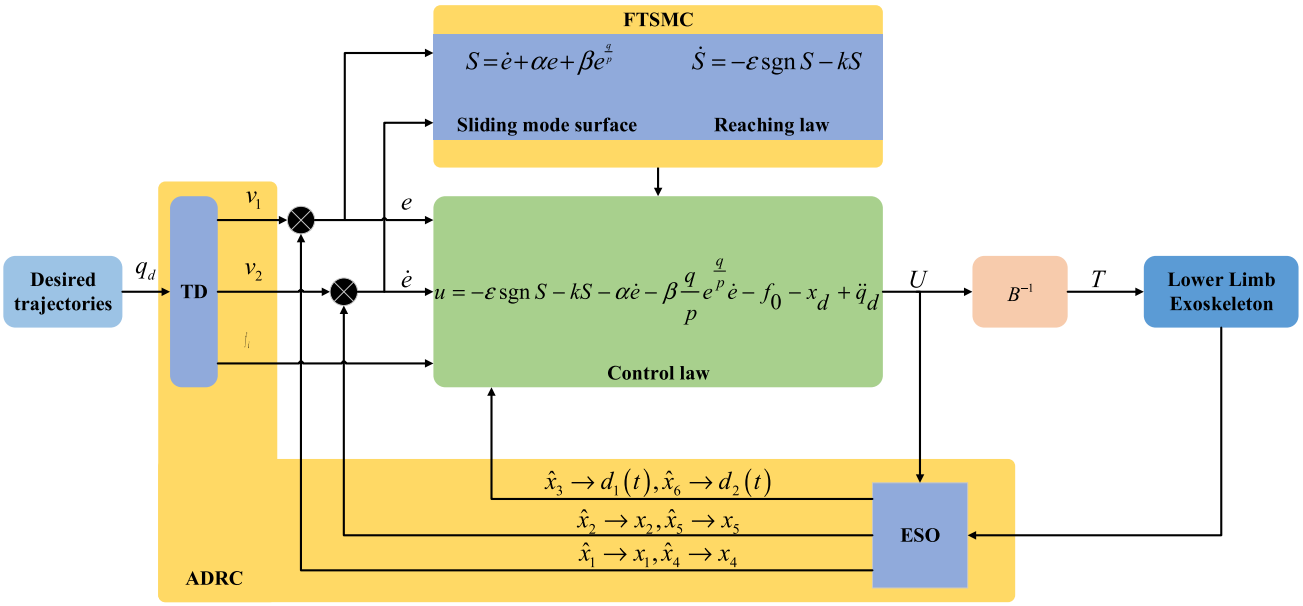

FIGURE 3. FTSMC compounded with ADRC designed for the lower limb exoskeleton.

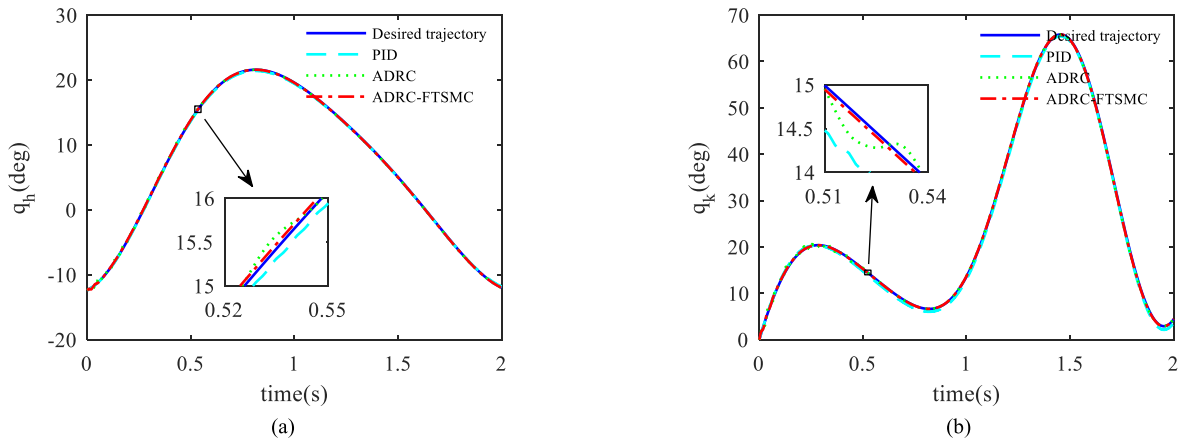

FIGURE 4. Tracking performance of PID, ADRC and ADRC-FTSMC in simulations. (a) Performance of the hip joint. (b) Performance of the knee joint.

TABLE 2. The exoskeleton parameters for simulation.

Parameters	Value	Unit
m_h	1.97	kg
m_k	0.93	kg
l_h	0.43	m
l_k	0.49	m
g	9.81	m/s^2

in Table 2. Table 3 shows the parameters of the proposed controller. In the simulation, the control law of PID controller is shown as follows,

$$u(t) = k_p e(t) + k_d \dot{e}(t) \tag{32}$$

where proportional parameter $k_p = 400$ and differential parameter $k_d = 50$ are obtained by parameter tuning. The parameters of ADRC in Eq. (19) are $w_0 = 900$, $k_p = 400$, and $k_d = 50$.

The tracking performance of the three control methods is shown in Fig. 4. It is obvious that the performance of the proposed hybrid control method and ADRC is better than PID. To make the difference more explicit, Fig. 5 shows the tracking error. Both the proposed method and ADRC reduce chattering significantly. Furthermore, the convergence speed of the proposed strategy has a distinct advantage over ADRC.

Table 4 illustrates the quantitative results of the same lower limb exoskeleton model with all three controllers. It is observed that the ADRC-FTSMC method provides superior control performance than others in the steady-state error.

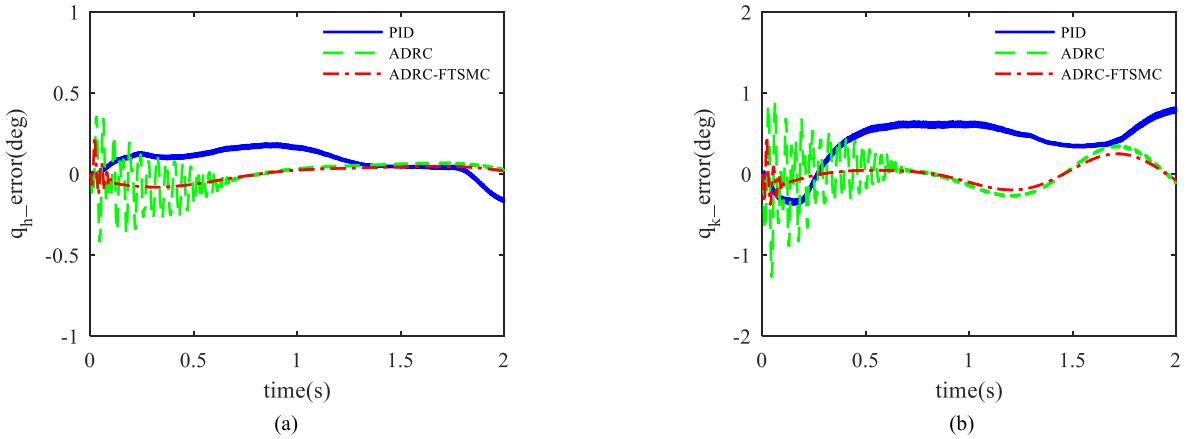

FIGURE 5. Tracking error comparison of PID, ADRC and ADRC-FTSMC in simulations. (a) Error comparison of the hip joint. (b) Error comparison of the knee joint.

TABLE 3. The parameters of ADRC-FTSMC.

Parameters	Value
w_0	900
r	10
h_0	0.001
q	5
p	9
α	10
β	5
ε	3
k	35
ξ	0.01

TABLE 4. Quantitative comparison.

Controllers	Ultimate Bound	Convergent Time
PID	0.87°	Infinite
ADRC	0.91°	0.69s
ADRC-FTSMC	0.47°	0.13s

Meanwhile, the convergence speed of the proposed control method is higher than ADRC.

V. EXPERIMENTS AND DISSCUSSIONS

A. EXPERIMENTAL SETUP

In order to further demonstrate the feasibility of the proposed strategy, we implemented the control law on the designed LLE. The experimental platform has some necessary auxiliary facilities, which includes embedded controller, driving module, power supply module, and data acquisition card. The embedded controller based on ARM-Cortex-A9 is used to run the control algorithm and send the motion commands. The control code is implemented in the Ubuntu operating system, with a sampling rate of 200Hz. The maxon DC motor and

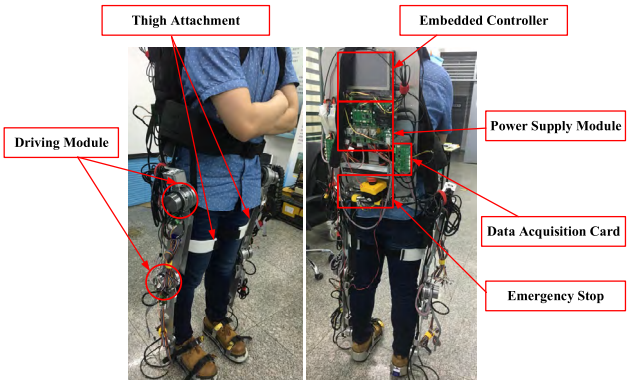

FIGURE 6. The subject wearing the LLE.

Elmo servo driver compose the driving module. The power is able to supply voltage of 5, 12, and 24 V. The data acquisition card collects the plantar pressure to determine the current phase. Fig. 6 shows the subject wearing the LLE.

The LLE control system mainly consists of the embedded controller, the sensor system and the actuation system, as shown in Fig. 7, which communicate with the modules via CAN (Controller Area Network) bus. The transmission rate of CAN bus is satisfied with the real-time request, which is up to 1 Mbit/s. Two CAN bus channels are set, where one is used for data collection while the other is for control instruction sending commands. To simplify the central control program, the control software is divided into three parts: the data acquisition module, the CAN bus module, and the control module. The CAN bus module includes the relevant files about communication protocol.

To protect the subject, the protective measures are taken into consideration in the hardware and software. Specifically, all the joints are equipped with mechanical limits to restrain the movement of the joints. As to the software, the control system will be closed when the detection driving current is exceeding the setting limit. Besides, the emergency stop is used to cut off the power supply in any emergency.

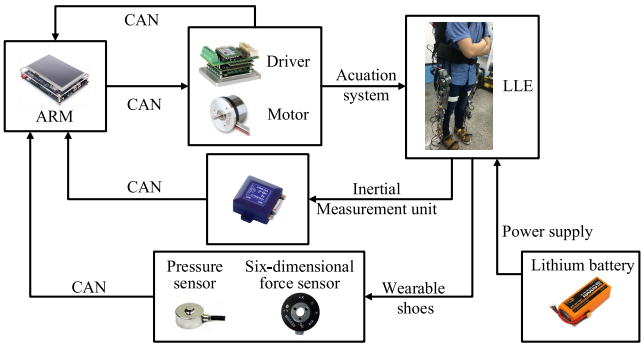

FIGURE 7. The control architecture of the LLE. The actuation system is consist of maxon DC motor and Elmo servo driver. The sensor system is compose of pressure sensor, six-dimensional force sensor, IMU and the optical encoder on the motor.

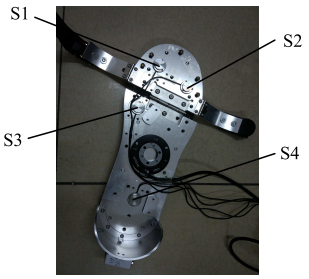

FIGURE 8. Pressure sensors in the wearable shoes. S1 placed in the hallux; S2 placed in the fourth metatarsus; S3 placed in the first metatarsus; S4 placed in the heel.

In the experiment, the pressure sensors in the wearable shoes are used to identify the walking phase [33], which can be divided into the stance phase and the swing phase. There are four pressure sensors on each foot as shown in Fig. 8, which are labeled as *S1*, *S2*, *S3* and *S4*. The pressure value of each sensor is defined as P_{S1}, P_{S2}, P_{S3} and P_{S4}. The rule for different walking phase identification is as follows,

$$\begin{cases} (P_{S1}+P_{S2}+P_{S3}+P_{S4})/4 > P_{S\,\min}, & \textit{stance phase} \\ (P_{S1}+P_{S2}+P_{S3}+P_{S4})/4 < P_{S\,\min}, & \textit{swing phase} \end{cases} \tag{33}$$

where $P_{S\min}$ is the minimum threshold. In the stance phase, the gravity compensation control approach is utilized to enable the legs to support the weight of the system. In the swing phase, the proposed method is used for trajectory control.

After identifying the walking phase, the human motion intention (HMI) is estimated by the six-dimensional force sensor that is embedded in the wearable shoes. Note that the research is focused on the swing leg in the sagittal plane, the HMI can be reflected by the vertical and horizontal forces that can be measured by the six-dimensional force sensor. The vertical force can state that the user want to lift up or put down his foot, and the horizontal force can state that the user want to move his foot forward or backward. In this article, the vertical force and the horizontal force are defined as F_Z and F_X. And the increment of the foot gait trajectory can be obtained as follows,

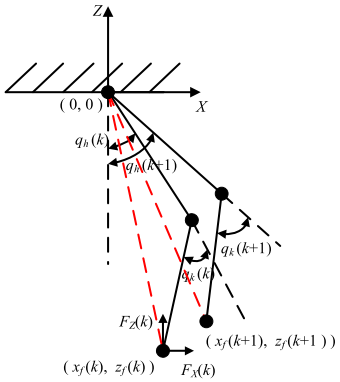

FIGURE 9. The schematic diagram of the LLE motion.

$$\Delta z_f(k) = \begin{cases} 0 & \|F_Z(k) - F_Z(0)\| < \alpha_z \\ \lambda_z(F_Z(k) - F_Z(0)) & \alpha_z < \|F_Z(k) - F_Z(0)\| < \beta_z \\ \Delta z_{f\,\max} & \|F_Z(k) - F_Z(0)\| > \beta_z \end{cases}$$
$$\Delta x_f(k) = \begin{cases} 0 & \|F_X(k) - F_X(0)\| < \alpha_x \\ \lambda_x(F_X(k) - F_X(0)) & \alpha_x < \|F_X(k) - F_X(0)\| < \beta_x \\ \Delta x_{f\,\max} & \|F_X(k) - F_X(0)\| > \beta_x \end{cases} \tag{34}$$

where Δz_f and Δx_f is the increment of the horizontal and the vertical increment respectively, $\alpha_f = [\alpha_z \alpha_x]$, $\beta_f = [\beta_z \beta_x]$, $\lambda_f = [\lambda_z \lambda_x]$ are constants, and $\Delta z_{f\,\max}$, $\Delta x_{f\,\max}$ are the maximum increment threshold. Therefore, the foot gait trajectory can be expressed as follows:

$$\begin{cases} z_f(k+1) = z_f(k) + \Delta z_f(k) \\ x_f(k+1) = x_f(k) + \Delta x_f(k) \end{cases} \tag{35}$$

To acquire the relation between the gait trajectory and the actuated joints (knee joint and hip joint) trajectory, we construct a simplified two-link model and establish its constraint equation. Since we mainly study the swinging legs, the trunk can be regarded as a fixed position. Besides, the ankle joint and the foot are integrated as the end of the model. Fig. 9 presented the schematic diagram of the LLE motion.

When the foot is at point k, the distance from coordinate origin to the end is $l(k)$; the hip joint angle is $q_h(k)$, and the knee joint angle is $q_k(k)$. The length of thigh and shank are l_h and l_k. From point k to point $k+1$, the increments of hip and knee joints can be expressed as follows.

$$\begin{aligned} \Delta q_h(k) = {} & \arctan(-\frac{x_f(k+1)}{z_f(k+1)}) + \arccos(\frac{l^2(k+1) + l_h^2 - l_k^2}{2 * l_h * l(k+1)}) \\ & - \arctan(-\frac{x_f(k)}{z_f(k)}) - \arccos(\frac{l^2(k) + l_h^2 - l_k^2}{2 * l_h * l(k)}) \\ \Delta q_k(k) = {} & (\pi - \arccos(\frac{l_h^2 + l_k^2 - l^2(k+1)}{2 * l_h * l_k})) \\ & - (\pi - \arccos(\frac{l_h^2 + l_k^2 - l^2(k)}{2 * l_h * l_k})) \end{aligned} \tag{36}$$

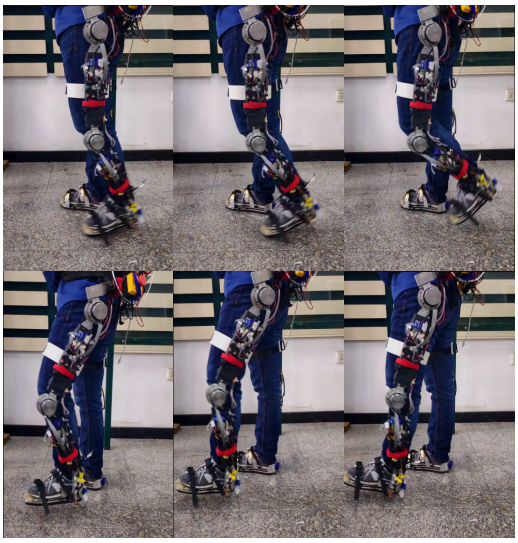

FIGURE 10. Volunteer wearing the LLE to follow the CGA trajectory.

The hip and knee joint trajectory can be generated as follows.

$$\begin{cases} q_h(k+1) = q_h(k) + \Delta q_h(k) \\ q_k(k+1) = q_k(k) + \Delta q_k(k) \end{cases} \tag{37}$$

Overall, hip and knee joint trajectory of the next point, can be obtained through Eq. (34) – Eq. (37). The trajectory reflects the human motion intention. The recognition result will be used to control the LLE in real time.

During the subject swinging leg, two modes are available, i.e., the passive motion mode (PMM) and the active motion mode (AMM). In the PMM, the subject's swing leg will follow the desired trajectory which is given by the CGA. For the AMM, it will follow the real-time trajectory generated by the HMI. The subject can switch the two modes by the trigger.

The process of wearing the LLE is as follows: (1) adjust the leg mechanism to fit the height of the user; (2) wear the LLE and fasten all belts to make the subject comfortable; (3) turn on the power supply to run all modules; (4) select the motion mode via the trigger switch; (5) press the start-up button of the control software when the subject tries to run. (6) lift up the left leg into swing phase.

B. EXPERIMENTAL RESULTS AND DISCUSSIONS

1) EXPERIMENT 1: PASSIVE MOTION MODE

In PMM experiments, the volunteer, a healthy 25-year-old man with weight 75.8kg and height 1.76m, wears the exoskeleton and moves his leg to follow the CGA trajectory. Before walking, the volunteer should adapt to the exoskeleton system under the security process. Since only the swing phase is concerned in the experiment, the volunteer is asked to shift his weight toward the right leg and swing the left leg. To evaluate the proposed method, the experiments were performed on the healthy subject by using PID, ADRC and the proposed control method ADRC-FTSMC, as shown in the Fig. 10.

TABLE 5. The error range of the hip joint and knee joint.

Controllers	Hip Joint	Knee Joint
PID	(-0.36°,0.22°)	(-1.98°,2.67°)
ADRC	(-0.33°,0.21°)	(-1.14°,0.36°)
ADRC-FTSMC	(-0.27°,0.17°)	(-0.53°,0.21°)

TABLE 6. The performance improvement of hip joint and knee joint.

Controllers	Hip Joint	Knee Joint
ADRC	33.1%	48.2%
ADRC-FTSMC	55.9%	81.9%

The parameters of the proposed controller are set as: $w_0 = 600$, $r = 10$, $h_0 = 0.001$, q = 5, p = 7, $\alpha = 10$, $\beta = 7$, $\varepsilon = 5$, $k = 27$, and $\xi = 0.01$. The gains of the PID controller are $k_p = 200$ and $k_d = 30$. The ADRC algorithm with parameters $w_0 = 600$, $k_p = 200$ and $k_d = 30$.

The knee and hip joint angles are monitored by the incremental encoder. Fig. 11 shows the tracking performance of the hip and the knee joint, which include the desired trajectory and three different real trajectories in five cycles. Fig. 12 gives the tracking error of the hip and the knee joints, where the error ranges of the hip joint and the knee joints are listed in Table 5. It can be seen that the tracking error based on the proposed method are smaller than those under the PID and ADRC control strategies. It is noticed that with a consideration of the convergence at ±5%, the convergent time of ADRC is1.15 sec while for ADRC-FTSMC is0.28 sec.

Fig.13 presented the comparison of the effectiveness of the PID, ADRC, and ADRC-FTSMC control methods by the root mean square error (*RMSE*) that is defined as follows,

$$RMSE = \sqrt{\frac{\sum_{k=1}^{N} e(k)^2}{N}} \tag{38}$$

where $e(k)$ is the tracking error and$N$ is the size of error vector.

To further evaluate the performance improvement (P_I) of three control method, the PID is considered as the standard and define P_I as follows,

$$P_I = \frac{RMSE_0 - RMSE_1}{RMSE_0} \times 100\% \tag{39}$$

where $RMSE_0 = [RMSE_{0P}, RMSE_{0P}]^T$ is the *RMSE* of PID control strategy and $RMSE_1 = [RMSE_{1A}, RMSE_{1AF}]^T$ is the *RMSE* of ADRC and ADRC-FTSMC control strategy. The $P_I$of hip joint and knee joint are shown in Table 6. Therefore, the proposed ADRC-FTSMC is capable of improving the human gait tracking performance.

2) EXPERIMENT 2: ACTIVE MOTION MODE

In the active mode, the six-dimensional force sensor is used to generate a gait trajectory through Eq. (34)-Eq. (37) based

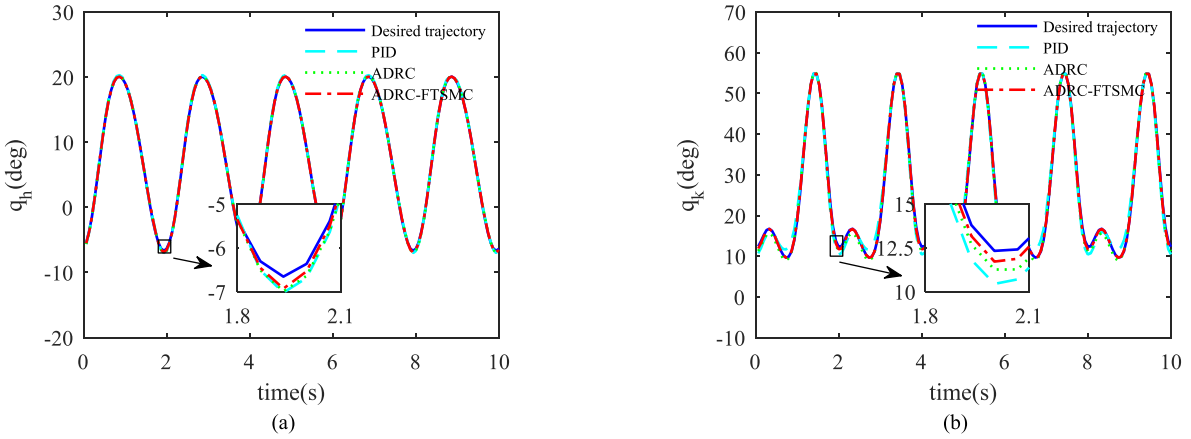

FIGURE 11. Trajectory tracking of hip joint and knee joint. (a) Performance of the hip joint. (b) Performance of the knee joint.

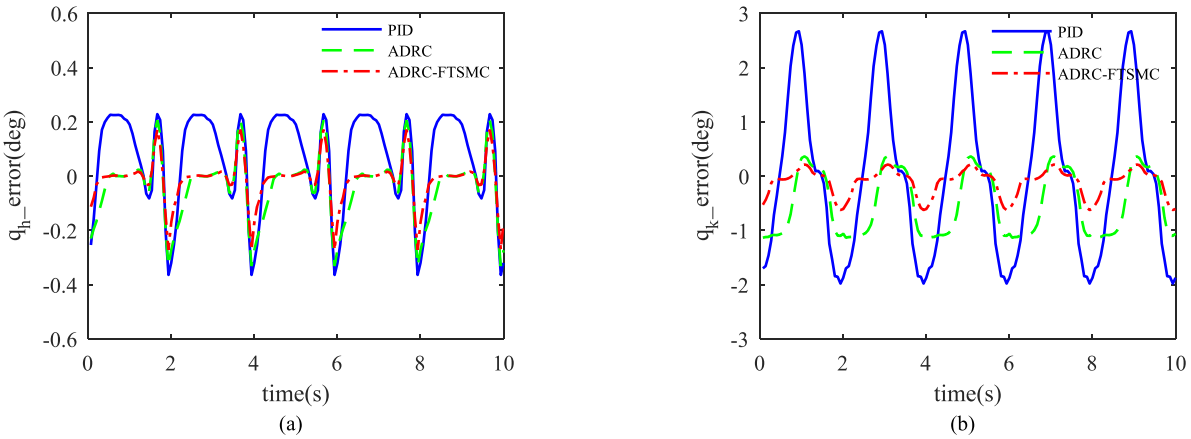

FIGURE 12. Trajectory error of hip joint and knee joint. (a) Tracking error of the hip joint. (b) Tracking error of the knee joint.

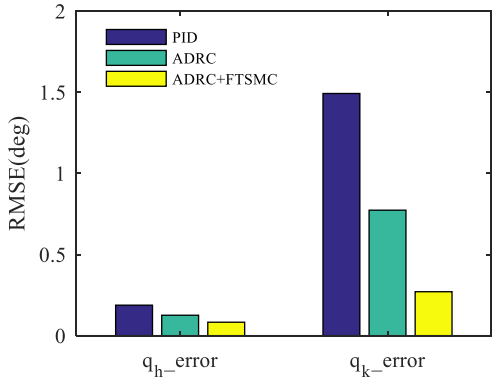

FIGURE 13. RSME comparison between the proposed method and the PID and ADRC control strategy.

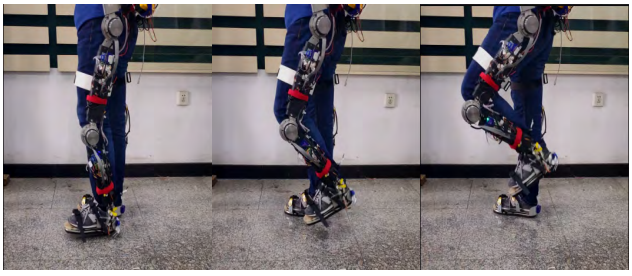

FIGURE 14. The participant move his feet up and down.

on the HMI in the swing phase. Since the PMM experiments has already shown the superiority of the proposed algorithm, the AMM experiments will mainly study the tracking performance of the real-time joint trajectories by using ADRC-FTSMC. The joint trajectories are generated online according to the HMI.

The experiments were performed on four healthy adult volunteers. Table 5 shows the data of the volunteers. All the volunteers were asked to move their feet up and down in a regular manner, as shown in the Fig. 14. The parameters of the proposed controller are set as: $w_0 = 600$, $r = 10$, $h_0 = 0.001$, $q = 3$, $p = 9$, $\alpha = 8$, $\beta = 5$, $\varepsilon = 3$, $k = 25$, and $\xi = 0.01$.

As presented before, the six-dimensional force sensor in the wearable shoes will detect the vertical and horizontal forces from volunteer's feet, which reflects the human motion intention. Fig. 15 shows the collected force signals from the

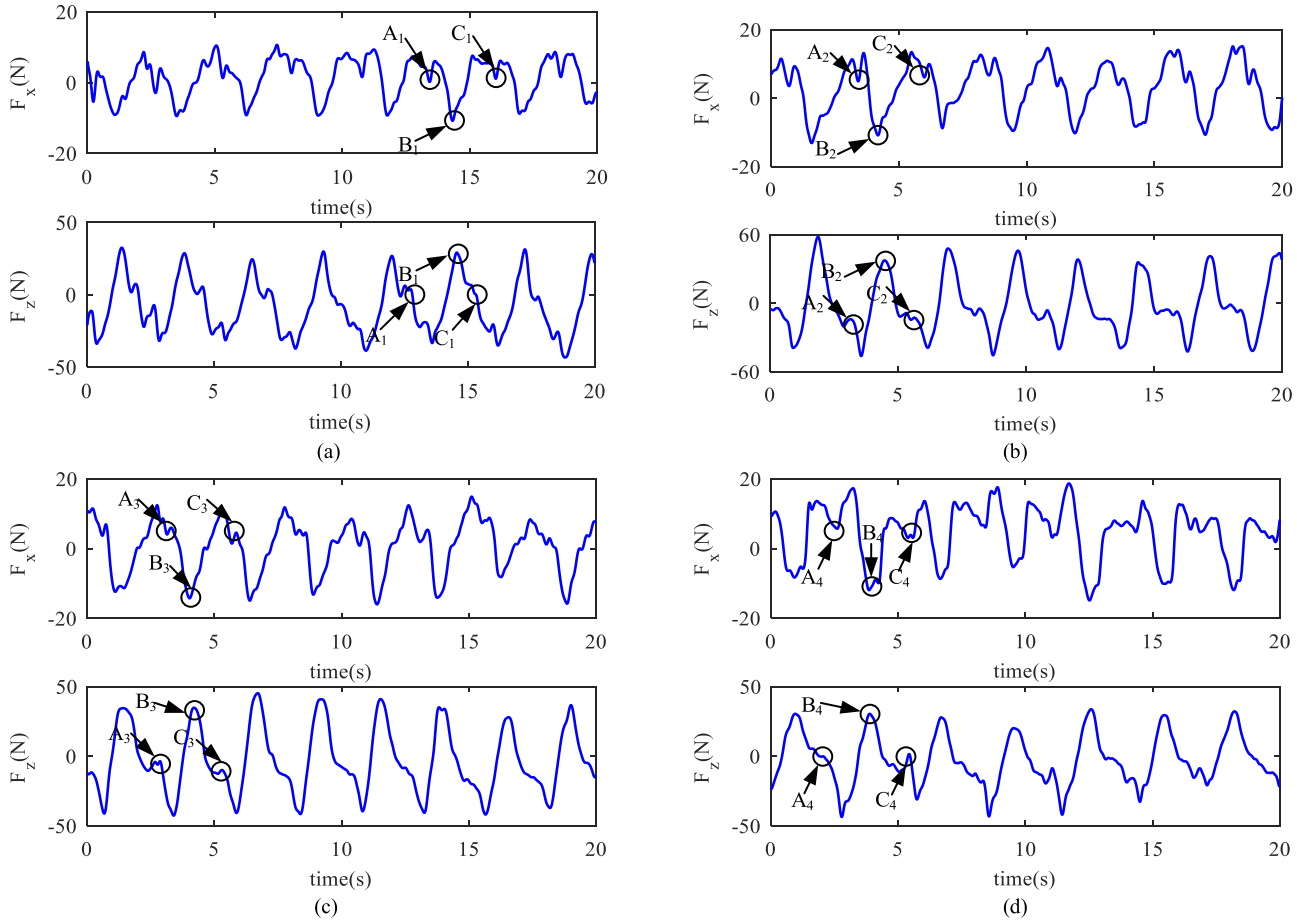

FIGURE 15. The vertical and horizontal force signal of four participants' feet in the active motion mode. (a) P1. (b) P2. (c) P3. (d) P4.

TABLE 7. Participant data.

Participant	P1	P2	P3	P4
Sex(M/F)	M	M	M	M
Age	25	23	25	29
Height(m)	1.76	1.82	1.79	1.77
Weight(kg)	75.8	81.2	70.8	78.1

four volunteers, based on which the desired hip and knee joint trajectories can be calculated by Eq. (34) – Eq. (37). Fig. 16 shows the acquired trajectories of hip and knee joints and the tracking performance under the proposed control method. In terms of overall tracking performance, the LLE can well track the estimated joint trajectory calculated from the vertical and horizontal force signal.

As shown in Fig. 15 and Fig. 16, the vertical and horizontal forces on the curve "A_i C_i" ($i = 1, 2, 3, 4$) is corresponding to hip and knee joints trajectory on the curve "A_iC_i", which is a cycle of the leg motion. The curve "A_iB_i" means the foot is lifted up and "B_iC_i" means moves down. In Fig. 16, we zoom in some regions of the trajectories and find the turning region has a large error relative to other positions. In addition, fluctuations exists in the rising and falling period, which results from the neglect of the ankle joint during the trajectory estimation. Despite this, the overall trend of motion estimation is correct.

In order to further evaluate the tracking performance of hip and knee joint, RMSE is used to compare the experimental results of the four participants, as shown in Fig. 17. The maximum and minimum RMSE of the hip joint are 0.25° and 0.47°, respectively. As for the knee joint, they are 0.83° and 1.28° respectively. These results have illustrated that the proposed ADRC-FTSMC method can also control the hip and knee joint to track the real-time trajectories well, which are generated by the HMI.

3) DISCUSSIONS

The above two experimental results exhibited the superiority of the proposed ADRC-FTSMC algorithm. In the PMM experiment, the proposed control method is used to track the CGA trajectory, which demonstrated that the proposed method is more accurate and faster compared with the conventional PID and the ADRC. In the AMM experiment, the proposed control method is used to track the real-time trajectory, which demonstrated that the proposed method could

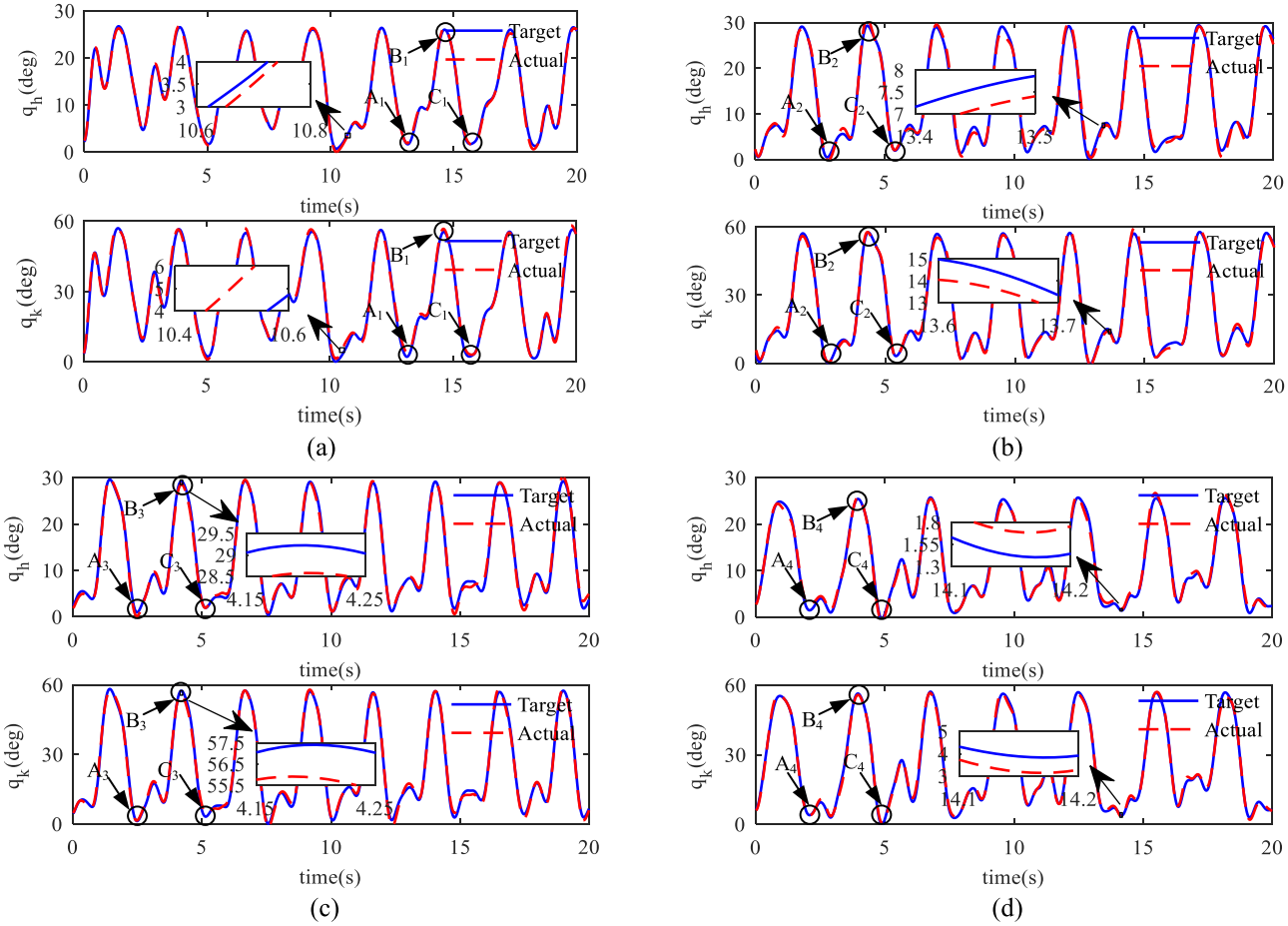

FIGURE 16. The desired hip joint and knee joint trajectories generated by the HMI and the tracking performance according to the proposed control method. (a) P1. (b) P2. (c) P3. (d) P4.

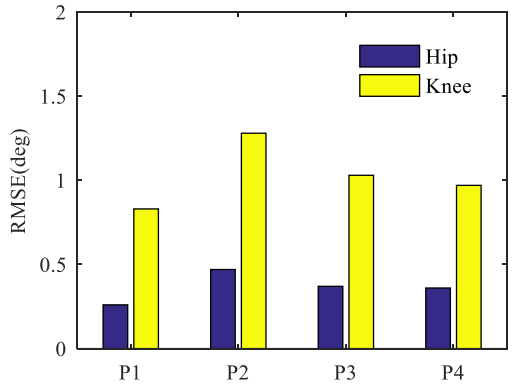

FIGURE 17. RSME comparison between the four participants.

adapt to different users and have a good practical application significance.

Meantime, we notice two drawbacks of the proposed method in practice. First, the parameters of the method need to adjust by empirical. This costs us too much time. Second, with the proposed method, the tracking performance of real-time trajectory is worse than the predefined CGA trajectory. There are two main reasons for those issues. One is that in the two-link model, which is used to calculate the real-time trajectory, the foot and ankle joints are considered as one object. The other one is the delay exits due to the real-time computation of human intentions identification.

VI. CONCLUSION AND FUTURE WORK

In this paper, the tracking control problem for an LLE has been presented. First, a mathematical model of the LLE is established. The system uncertainty and external disturbance are replaced by lumped disturbance to decouple the MIMO system. Then, the ADRC associated with FTSMC controller has been proposed to reject disturbance and converge to a bounded region in finite time. The proposed method is tested by simulations and experiment studies with two modes. In the PMM, the proposed controller is more accurate and faster compared to the conventional PID controller and ADRC strategy. In the AMM, the proposed method also performed well in the real-time trajectory experiments, where the trajectory information are obtained by the six-dimensional force sensor in the wearable shoes. In conclusion, the proposed method can help the LLE obtain higher level of control quality through more precise tracking and rapid response.

In future, we will study the parameters self-tuning method, which is significant in practical application. Furthermore we will build an accurate model with consideration of the ankle joint for the estimation of the human motion intention. Besides, the data processing and the calculation ability needs to be improved, which can accelerate the transmission speed and reduce latency in online situation. Since this paper mainly focuses on the control of LLE in the swing phase, we will extend this proposed method to other situations in the future, such as standing and sitting.

ACKNOWLEDGMENT

The authors would like to thank the reviewers and the editor for their constructive remarks and suggestions for improving this paper.

REFERENCES

[1] T. Yan, M. Cempini, C. M. Oddo, and N. Vitiello, "Review of assistive strategies in powered lower-limb orthoses and exoskeletons," *Robot. Auto. Syst.*, vol. 64, pp. 120–136, Feb. 2015.
[2] A. J. Young and D. P. Ferris, "State of the art and future directions for lower limb robotic exoskeletons," *IEEE Trans. Neural Syst. Rehabil. Eng.*, vol. 25, no. 2, pp. 171–182, Feb. 2017.
[3] J. Ghan and H. Kazerooni, "System identification for the Berkeley Lower Extremity Exoskeleton (BLEEX)," in *Proc. IEEE Int. Conf. Robot. Automat.*, Orlando, FL, USA, May 2006, pp. 3477–3484.
[4] H. Kazerooni, R. Steger, and L. Huang, "Hybrid control of the Berkeley lower extremity exoskeleton (BLEEX)," *Int. J. Robot. Res.*, vol. 25, nos. 5–6, pp. 561–573, May/Jun. 2006.
[5] Y. Sankai, *HAL: Hybrid Assistive Limb Based on Cybernics*, vol. 66. Berlin, Germany: Springer, 2011, pp. 25–34.
[6] G. Aguirre-Ollinger, J. E. Colgate, M. A. Peshkin, and A. Goswami, "Design of an active one-degree-of-freedom lower-limb exoskeleton with inertia compensation," *Int. J. Robot. Res.*, vol. 30, no. 4, pp. 486–499, Apr. 2011.
[7] W. Meng, Q. Liu, Z. Zhou, and A. Qingsong, "Active interaction control applied to a lower limb rehabilitation robot by using EMG recognition and impedance model," *Ind. Robot, Int. J. Robot. Res.*, vol. 41, no. 5, pp. 465–479, Aug. 2014.
[8] H. Kazerooni, J. L. Racine, L. Huang, and R. Steger, "On the control of the Berkeley Lower Extremity Exoskeleton (BLEEX)," in *Proc. IEEE Int. Conf. Intell. Robots Syst.*, Barcelona, Spain, Apr. 2005, pp. 4353–4360.
[9] D. Sanz-Merodio, M. Cestari, J. C. Arevalo, and E. Garcia, "Control motion approach of a lower limb orthosis to reduce energy consumption," *Int. J. Adv. Robotic Syst.*, vol. 9, no. 6, p. 232, Dec. 2012.
[10] H. K. Kwa, J. H. Noorden, M. Missel, T. Craig, P. D. Neuhaus, and J. E. Pratt, "Development of the IHMC mobility assist exoskeleton," in *Proc. IEEE Int. Conf. Robot. Automat.*, Kobe, Japan, May 2009, pp. 2556–2562.
[11] L. K. Wang, Z. J. Du, W. Dong, Y. Shen, and G. Y. Zhao, "Intrinsic sensing and evolving internal model control of compact elastic module for a lower extremity exoskeleton," *Sensors*, vol. 18, no. 3, p. 909, 2018.
[12] Y. Long, Z. Du, C. Chen, W. Wang, L. He, X. Mao, G. Xu, G. Zhao, and X. Li "Development and analysis of an electrically actuated lower extremity assistive exoskeleton," *J. Bionic Eng.*, vol. 14, no. 2, pp. 272–283, Jun. 2017.
[13] H.-B. Kang and J.-H. Wang, "Adaptive control of 5 DOF upper-limb exoskeleton robot with improved safety," *ISA Trans.*, vol. 52, no. 6, pp. 844–852, Nov. 2013.
[14] Z. Li, C.-Y. Su, G. Li, and H. Su, "Fuzzy approximation-based adaptive backstepping control of an exoskeleton for human upper limbs," *IEEE Trans. Fuzzy Syst.*, vol. 23, no. 3, pp. 555–566, Jun. 2015.
[15] K. Kong and D. Jeon, "Design and control of an exoskeleton for the elderly and patients," *IEEE/ASME Trans. Mechatronics*, vol. 11, no. 4, pp. 428–432, Aug. 2006.
[16] Y. Long, Z.-J. Du, W.-D. Wang, and W. Dong, "Robust sliding mode control based on GA optimization and CMAC compensation for lower limb exoskeleton," *Appl. Bionics Biomech.*, vol. 2016, Feb. 2016, Art. no. 5017381.
[17] Z. Li, C.-Y. Su, G. Li, and H. Su, "Fuzzy approximation-based adaptive backstepping control of an exoskeleton for human upper limbs," *IEEE Trans. Fuzzy Syst.*, vol. 23, no. 3, pp. 555–556, Jun. 2015.
[18] R. Lu, Z. Li, C.-Y. Su, and A. Xue, "Development and learning control of a human limb with a rehabilitation exoskeleton," *IEEE Trans. Ind. Electron.*, vol. 61, no. 7, pp. 3776–3785, Jul. 2014.
[19] Y. Huang and W. Xue, "Active disturbance rejection control: Methodology and theoretical analysis," *ISA Trans.*, vol. 53, no. 4, pp. 963–976, 2014.
[20] J. Han, "From PID to active disturbance rejection control," *IEEE Trans. Ind. Electron.*, vol. 56, no. 3, pp. 900–906, Mar. 2009.
[21] Y. Long, Z. Du, L. Cong, W. Wang, W. Dong, and Z. Zhang, "Active disturbance rejection control based human gait tracking for lower extremity rehabilitation exoskeleton," *ISA Trans.*, vol. 67, pp. 389–397, Mar. 2017.
[22] R. Li, T. Li, R. Bu, Q. Zheng, and C. L. P. Chen, "Active disturbance rejection with sliding mode control based course and path following for underactuated ships," *Math. Problems Eng.*, vol. 2013, Sep. 2013, Art. no. 743716.
[23] T.-J. Su, S.-M. Wang, J. S.-H. Tsai, T.-Y. Tsou, and V.-K. Tran, "Design of fuzzy and linear active disturbance rejection control for insulin infusion in type 1 diabetic patients," *Int. J. Fuzzy Syst.*, vol. 19, no. 6, pp. 1966–1977, Dec. 2017.
[24] M. Ali and L. Mehennaoui, "Active disturbance rejection control of a SCARA robot arm," *Int. J. U-E-Service, Sci. Technol.*, vol. 8, no. 1, pp. 435–446, 2015.
[25] Y. Qi, C. B. Soh, E. Gunawan, K.-S. Low, and R. Thomas, "Assessment of foot trajectory for human gait phase detection using wireless ultrasonic sensor network," *IEEE Trans. Neural Syst. Rehabil. Eng.*, vol. 24, no. 1, pp. 88–97, Jan. 2016.
[26] J. J. Craig, *Introduction to Robotics: Mechanics and Control*. New York, NY, USA: Pearson Education, 1986.
[27] M. W. Spong, S. Hutchinson, and M. Vidyasagar, *Robot Modeling and Control*. New York, NY, USA: Industrial Robot An International Journal, 2006.
[28] Z. Gao, "Scaling and bandwidth-parameterization based controller tuning," in *Proc. Amer. Control Conf.*, Denver, CO, USA, Jun. 2003, pp. 4989–4996.
[29] J. Liu and X. Wang, *Advanced Sliding Mode Control for Mechanical Systems*. Berlin, Germany: Springer, 2012.
[30] Y. Feng, X. Yu, and Z. Man, "Non-singular terminal sliding mode control of rigid manipulators," *Automatica*, vol. 38, no. 12, pp. 2159–2167, 2002.
[31] Y. Shtessel, C. Edwards, L. Fridman, and A. Levant, *Sliding Mode Control and Observation*. New York, NY, USA: Springer, 2014.
[32] R. Madoński and P. Herman, "Survey on methods of increasing the efficiency of extended state disturbance observers," *ISA Trans.*, vol. 56, pp. 18–27, May 2015.
[33] Y. Long, Z.-J. Du, W.-D. Wang, G.-Y. Zhao, G.-Q. Xu, L. He, X.-W. Mao, and W. Dong, "PSO-SVM-based online locomotion mode identification for rehabilitation robotic exoskeletons," *Sensors*, vol. 16, no. 9, p. 1408, Sep. 2016.

CHAO-FENG CHEN received the B.S. degree from Yanshan University, in 2013, and the M.S. degree from the Harbin Institute of Technology, China, in 2016, where he is currently pursuing the Ph. D degree. His research interests include wearable robots, mechanical rehabilitation device, and machine learning.

ZHI-JIANG DU (M'05) received the B.S. degree in mechanical engineering and the M.S. and Ph.D. degrees in mechatronics engineering and from the Harbin Institute of Technology (HIT), in 1995, 1997, and 2001, respectively, where he is currently with the State Key Laboratory of Robotics and System. He has been a Professor of mechatronics engineering, since 2006. His research interests include the general areas of medical robots, industrial robots, and special robots.

LONG HE is currently with the Weapon Equipment Research Institute, China South Industries Group Corporation, China. He is a Senior Engineer. His research interests include the general areas of mechanical design and optimization, wearable exoskeleton, and special robots.

JIA-QI WANG received the B.S degree from the Harbin Institute of Technology, in 2017, where she is currently pursuing the Ph.D. degree. Her research interest includes robotics, especially exoskeletons.

DONG-MEI WU received the Ph.D. degree in mechatronic engineering from the Harbin Institute of Technology, China, in 2003, where she is currently a Professor. Her research interests include medical robots, as well as robotic system integration and simulation technology.

WEI DONG (M'05–SM'16) received the B.S. degree in mechanical engineering and the M.S. and Ph.D. degrees in mechatronics engineering from the Harbin Institute of Technology (HIT), in 2001, 2003, and 2007, respectively. He was a Postdoctoral Researcher with the University of Connecticut, USA, from 2007 to 2009, and CNRS FEMTO-ST, France, from 2009 to 2010. He has extensive experience in a series of inter-related research subjects, including innovative design of robot/mechatronics systems, robotic system modeling and optimization, and smart material and structure integration and their application. He is currently with the State Key Laboratory of Robotics and System, HIT. His research interests include the general areas of robotics and mechatronics.